Hydroclimatic variability of opposing late Pleistocene climates in the Levant revealed by deep Dead Sea sediments; Appendices

Yoav Ben Dor[1], Francesco Marra[1,2], Moshe Armon[1], Yehouda Enzel[1], Efrat Morin[1]

1 The Fredy and Nadine Herrmann Institute of Earth Sciences, The Hebrew University of Jerusalem, Jerusalem, 9190501, Israel
2 Institute of Atmospheric Sciences and Climate, National Research Council of Italy, Bologna, 40129, Italy

Correspondence to: Yoav Ben Dor (Yoav.Bendor1@mail.huji.ac.il)

Supplementary 1 - figures

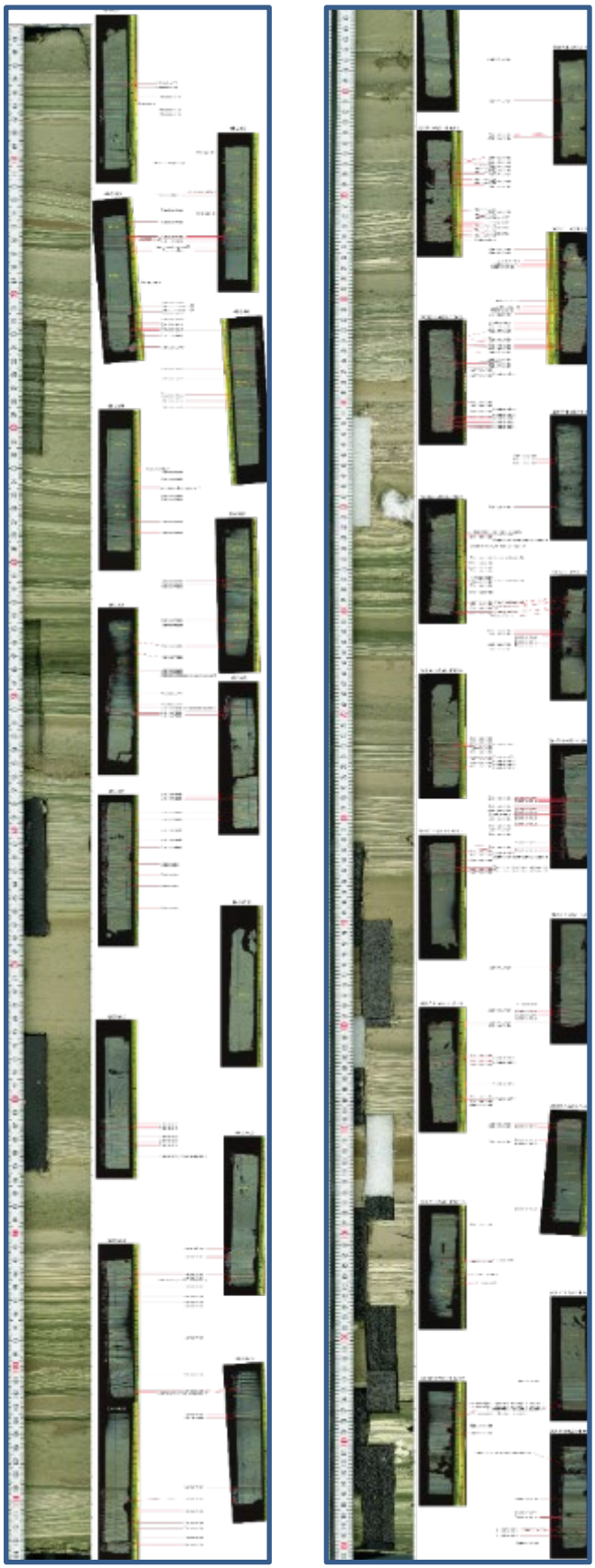

Figure S1 – varve counting and microfacies description of the two studied core sections. left: core section 48-2 deposited during lake level fall, right: core section 51-1 deposited during lake level rise.

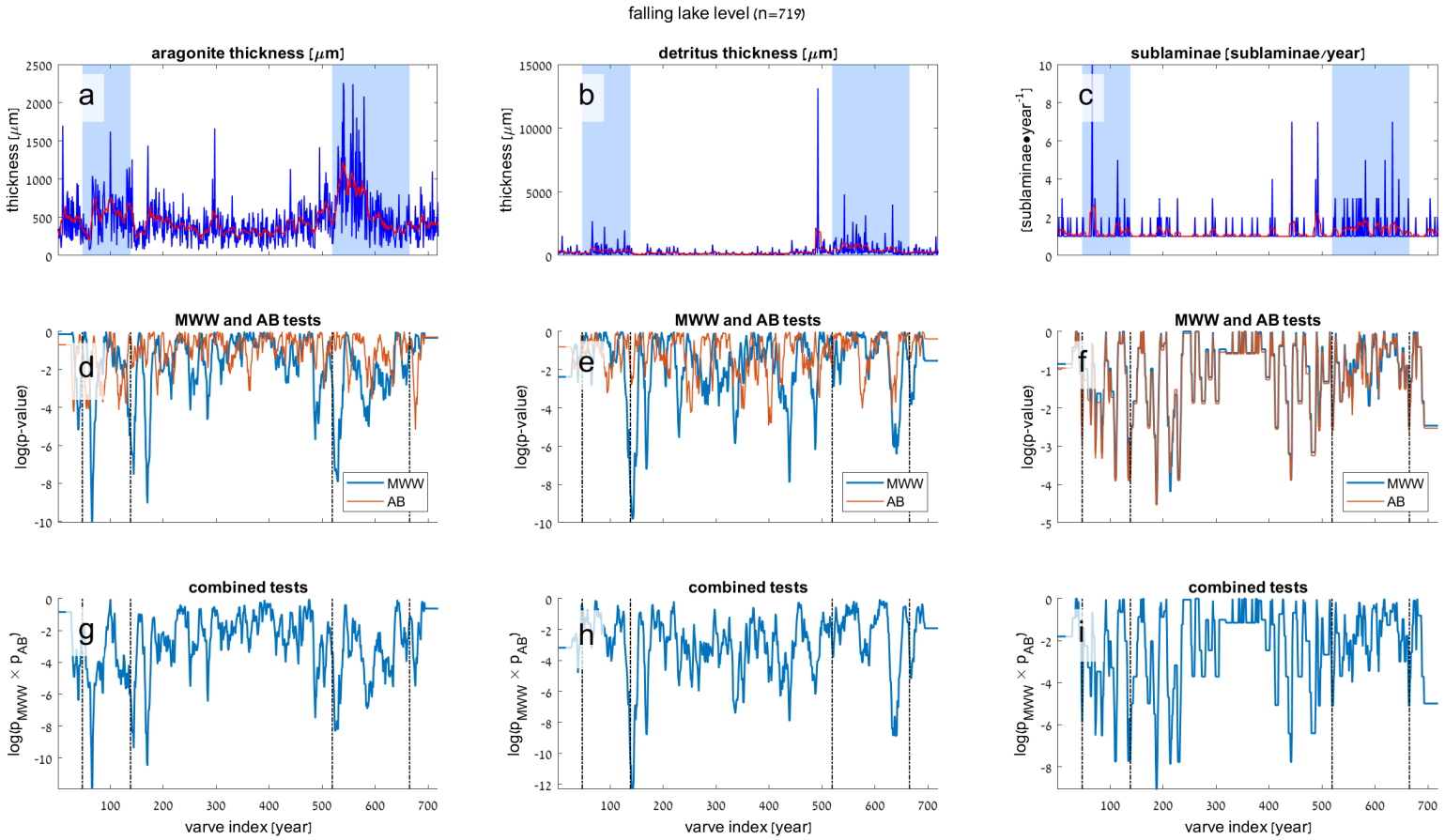

Figure S2 –data and statistical analysis of sediments microfacies analyses during lake level fall. (a) thickness of aragonite laminae, (b) thickness of detrital laminae and (c) flood frequency. d-f – log of p-value of running Mann-Whitney-Wilcoxon (MWW) and Ansari-Bradley (AB) tests with a window size of 100 years (50 years in each direction). g-i – log of the p-values products of the MWW and the AB tests calculated as $log(p_{MWW} \cdot p_{AB})$. Blue rectangles indicate possible cluster of intense flood frequency that also statistically significant shifts identified using the combined MWW and AB tests.

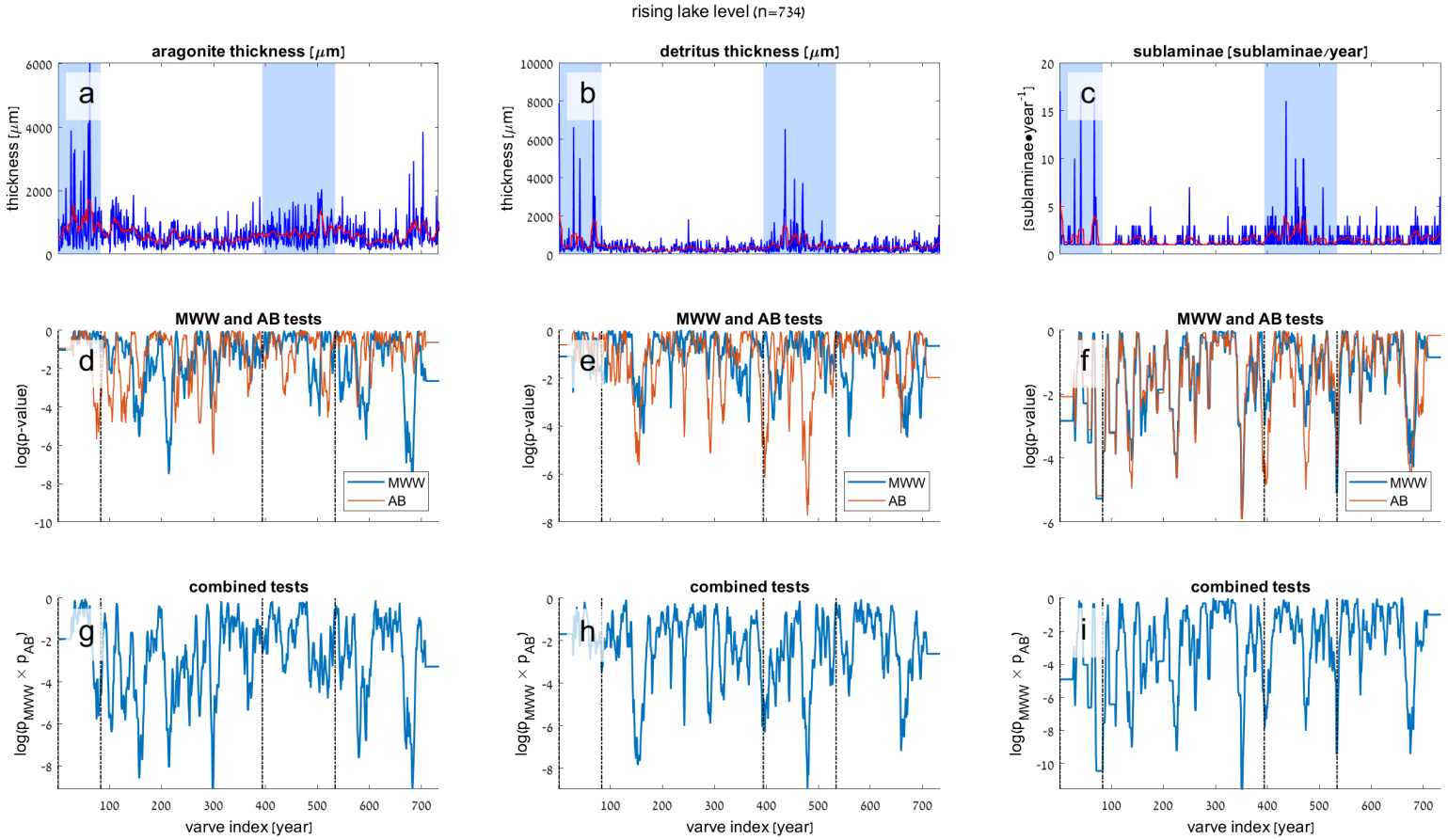

Figure S3 – data and statistical analysis of sediments microfacies analyses during lake level rise. (a) thickness of aragonite laminae, (b) thickness of detrital laminae and (c) flood frequency. d-f – log of p-value of running Mann-Whitney-Wilcoxon (MWW) and Ansari-Bradley (AB) tests with a window size of 100 years (50 years in each direction). g-i – log of the p-values products of the MWW and the AB tests calculated as $log(p_{MWW} \cdot p_{AB})$. Blue rectangles indicate possible cluster of intense flood frequency that also statistically significant shifts identified using the combined MWW and AB tests.

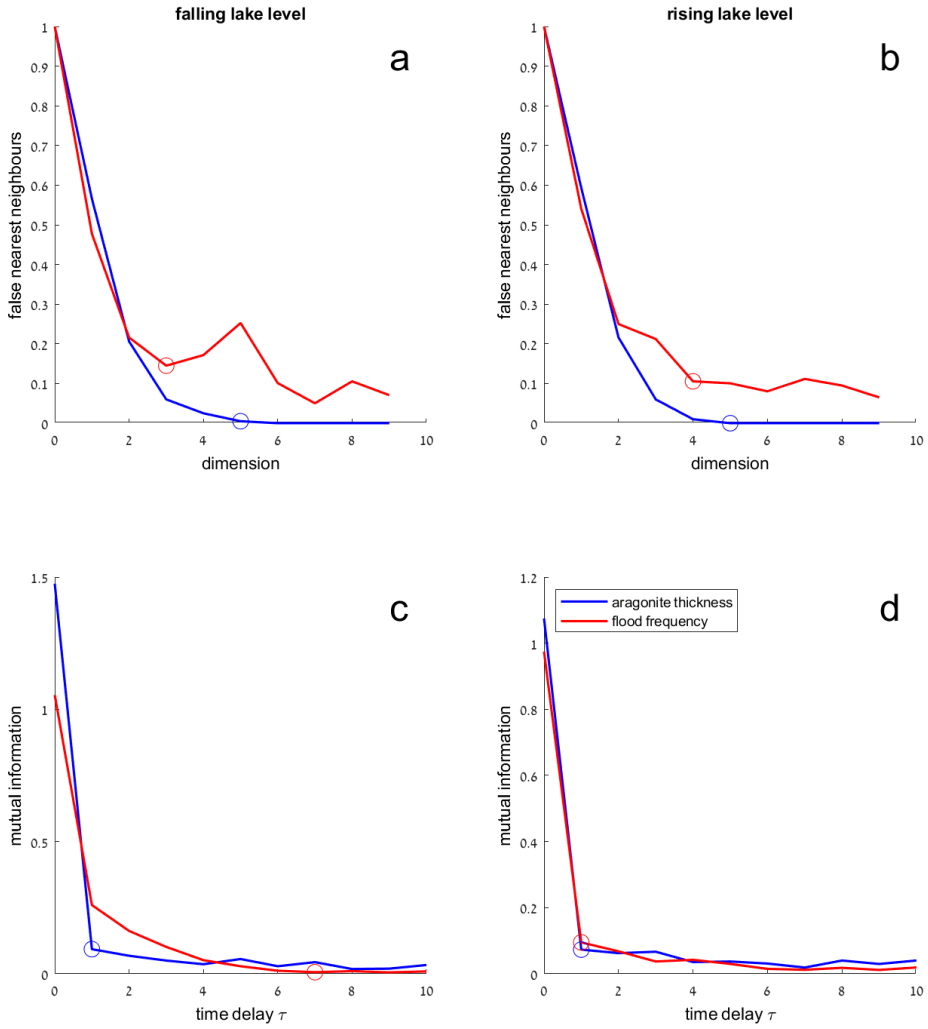

Figure S4 –(a,b) False nearest neighbors analyses of aragonite (blue) and flood frequency (red) during falling (a) and rising (b) lake level. The analyses were performed over the rescaled and normalized data after detrending removing the 1st SSA reconstructed component. (c,d) Results of mutual information analyses of aragonite and flood frequency during falling (c) and rising (d) lake level. The selected parameters for the recurrence analyses are marked with a circle.

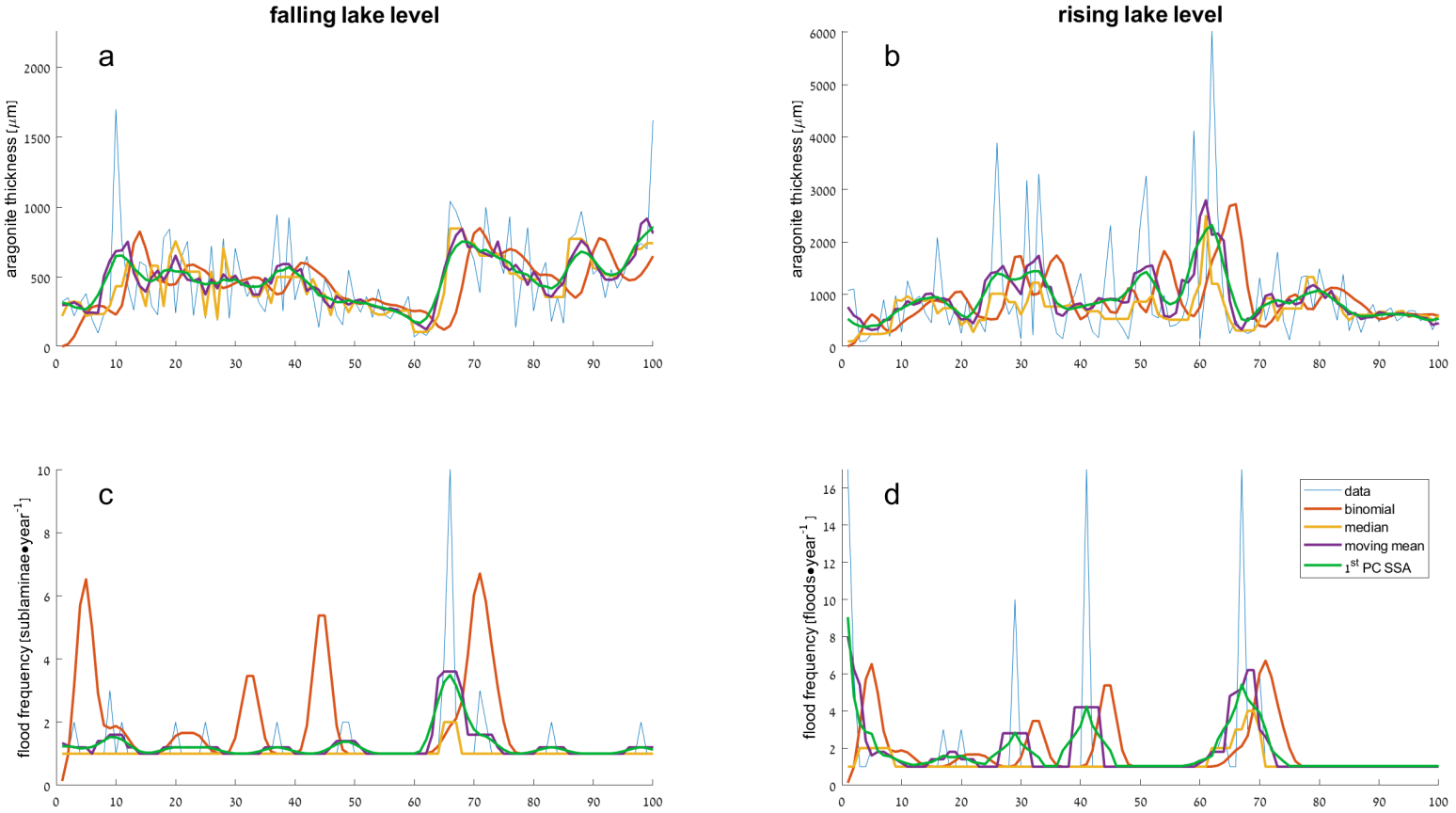

Figure S5 – the effect of multiple smoothing filters (window width 5 years) applied on the time series of aragonite laminae thickness (a,b) and flood frequency (c,d) for the falling (a,c) and rising (b,d) lake levels. Note the phase lag generated by the binomial filter (Marchand and Marmet, 1983), the undershooting of values by the median filter, and the inherent noisiness of the moving mean. The 1st reconstructed component of the singular spectrum analysis (SSA) (Broomhead and King, 1986; Ghil et al., 2002) follows the trend without a phase shift and was selected for smoothing for further analyses.

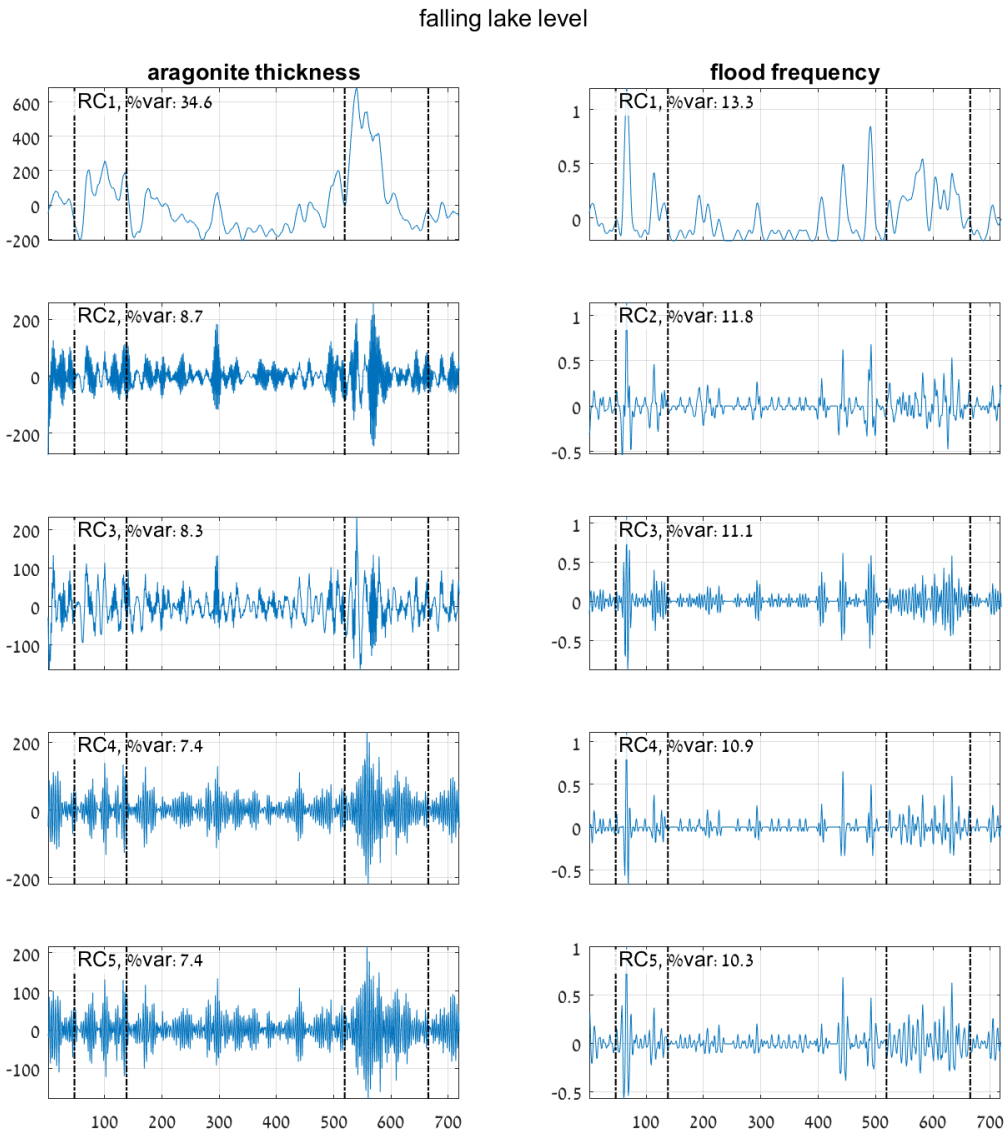

Figure S6 – singular spectrum analyses of aragonite thickness (left) and flood frequency (right) during lake level fall. The rows depict the reconstructed components (RC) 1-5. The % of explained variance is noted for each reconstructed component. Dashed black lines depict possible identified cluster.

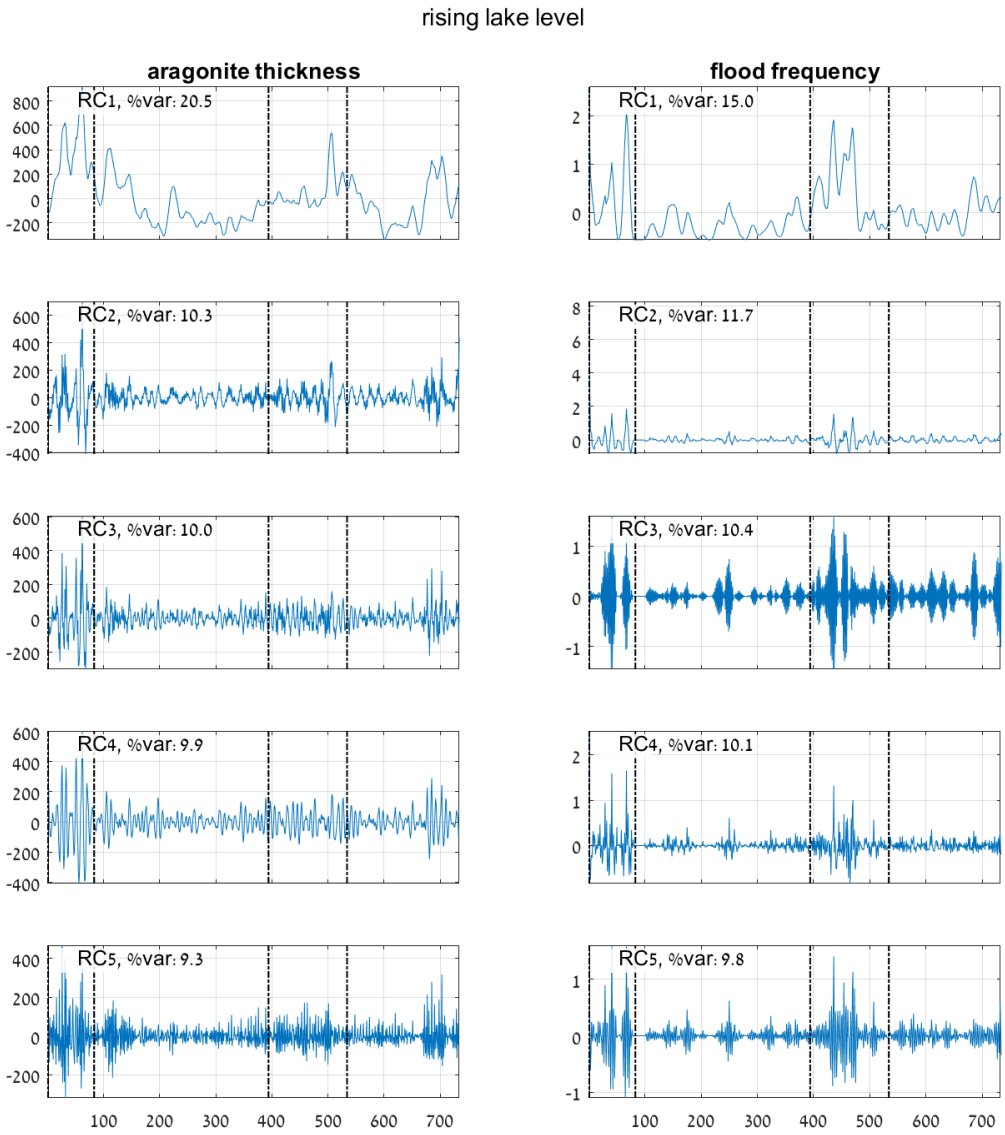

Figure S7 – singular spectrum analyses of aragonite thickness (left) and flood frequency (right) during lake level rise. The rows depict the reconstructed components (RC) 1-5. The % of explained variance is noted for each reconstructed component. Dashed black lines depict possible identified cluster.

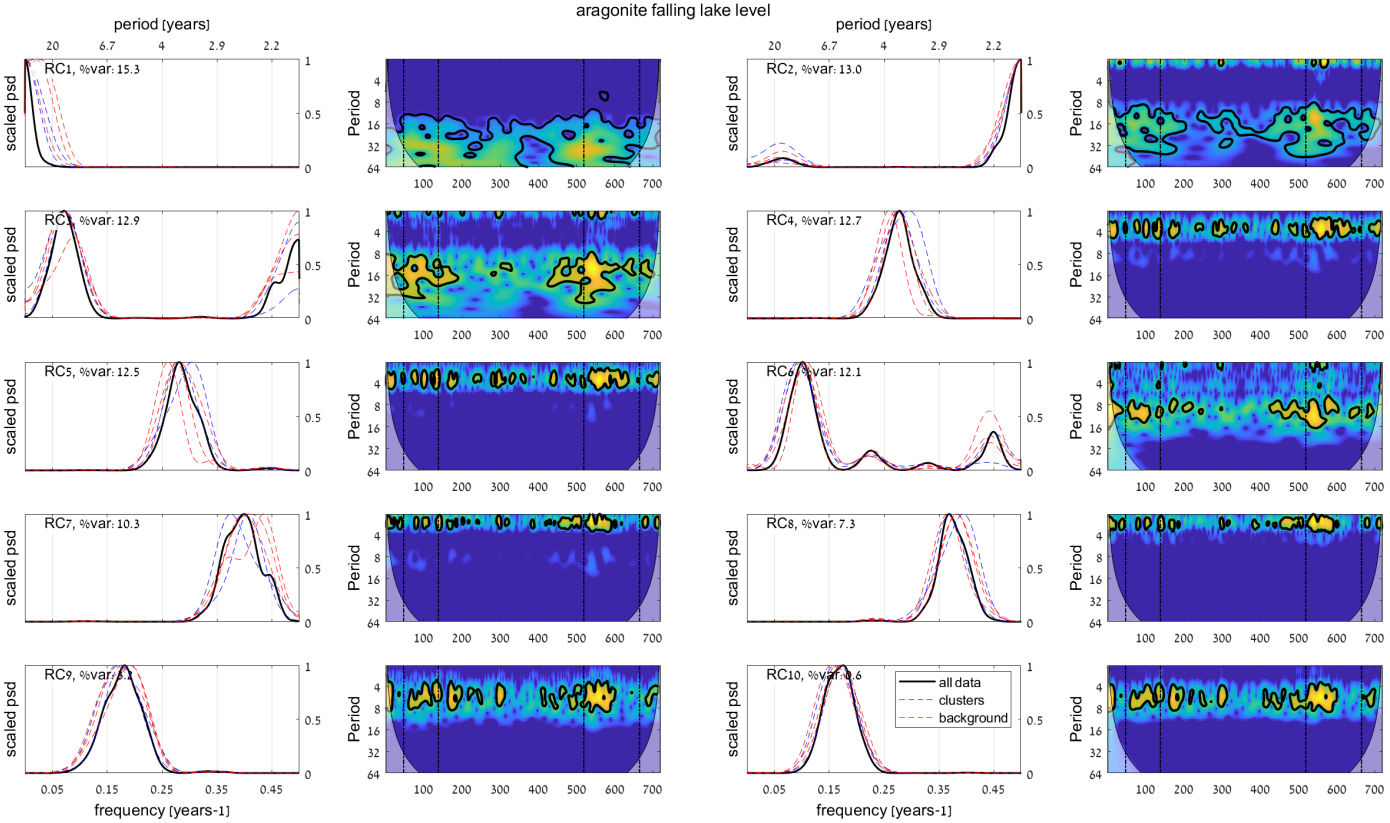

Figure S8 – Welch periodogram and wavelet analyses for the SSA RCs 1-10 of aragonite thickness data during lake level fall. The periodograms were calculated using a Hamming window of 25 years length with 50% overlap, and wavelet analyses were carried out after normalizing to zero mean and a unity standard deviation.

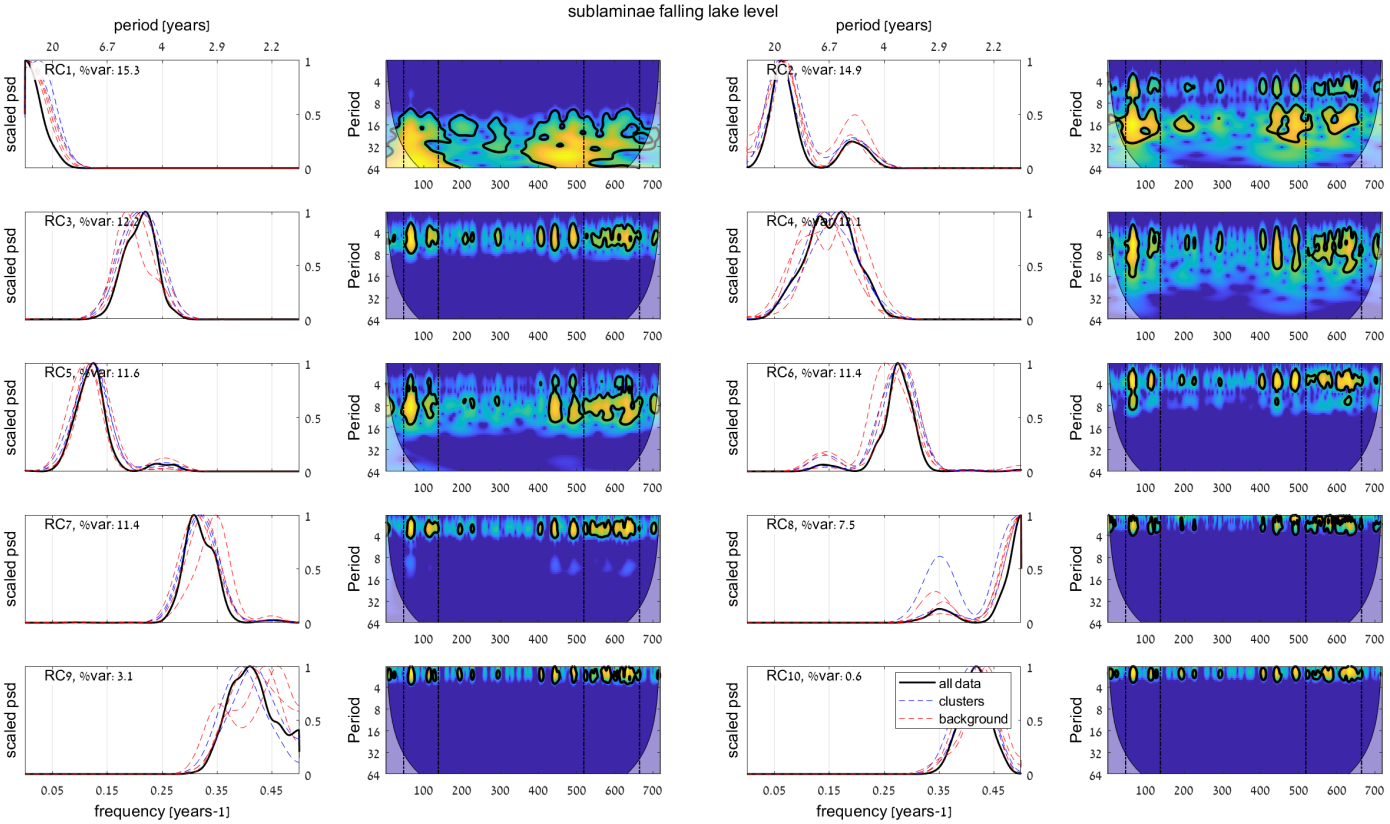

Figure S9 – Welch periodogram and wavelet analyses for the SSA RCs 1-10 of the sublaminae data during lake level fall. The periodograms were calculated using a Hamming window of 25 years length with 50% overlap, and wavelet analyses were carried out after normalizing to zero mean and a unity standard deviation.

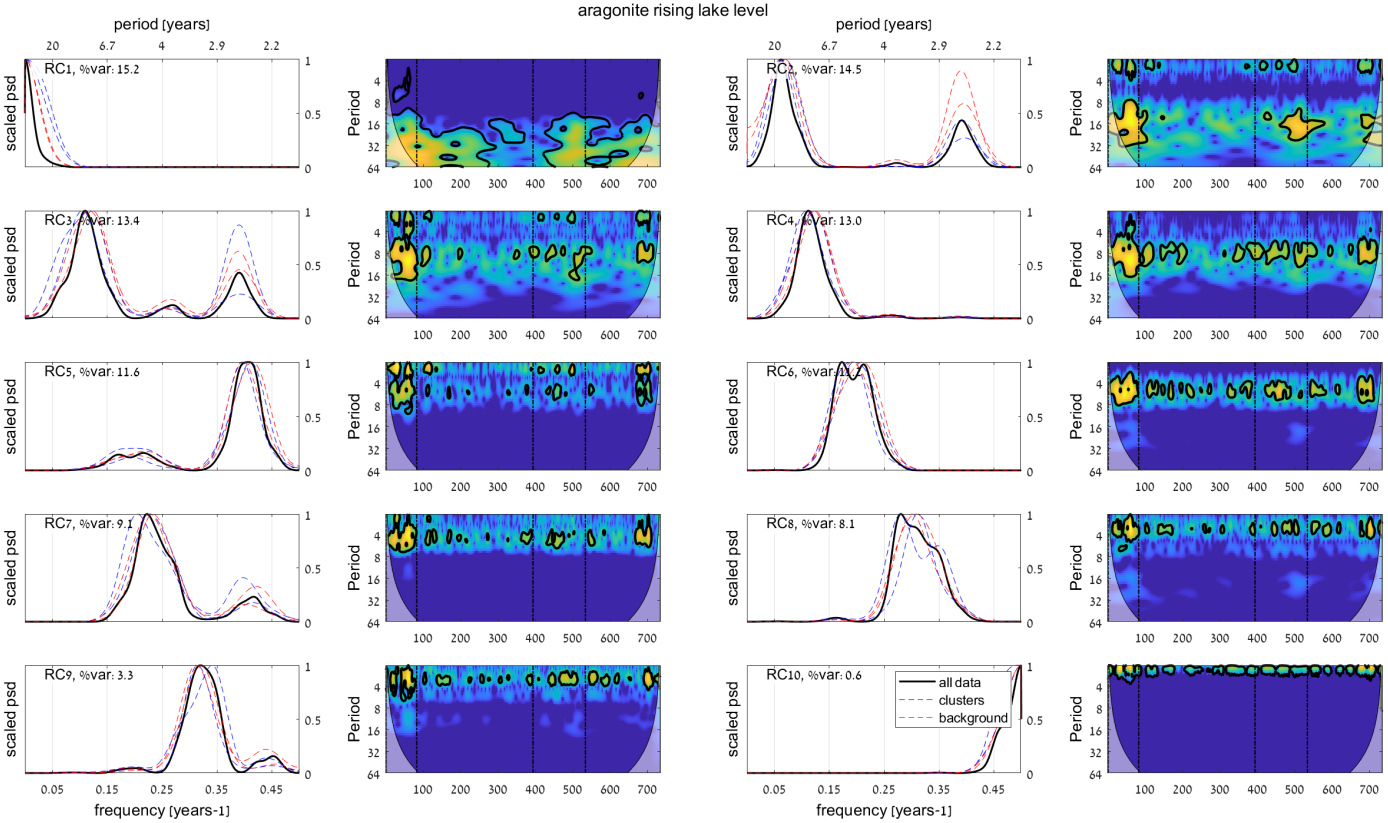

Figure S10 – Welch periodogram and wavelet analyses for the SSA RCs 1-10 of the aragonite thickness data during lake level rise. The periodograms were calculated using a Hamming window of 25 years length with 50% overlap, and wavelet analyses were carried out after normalizing to zero mean and a unity standard deviation.

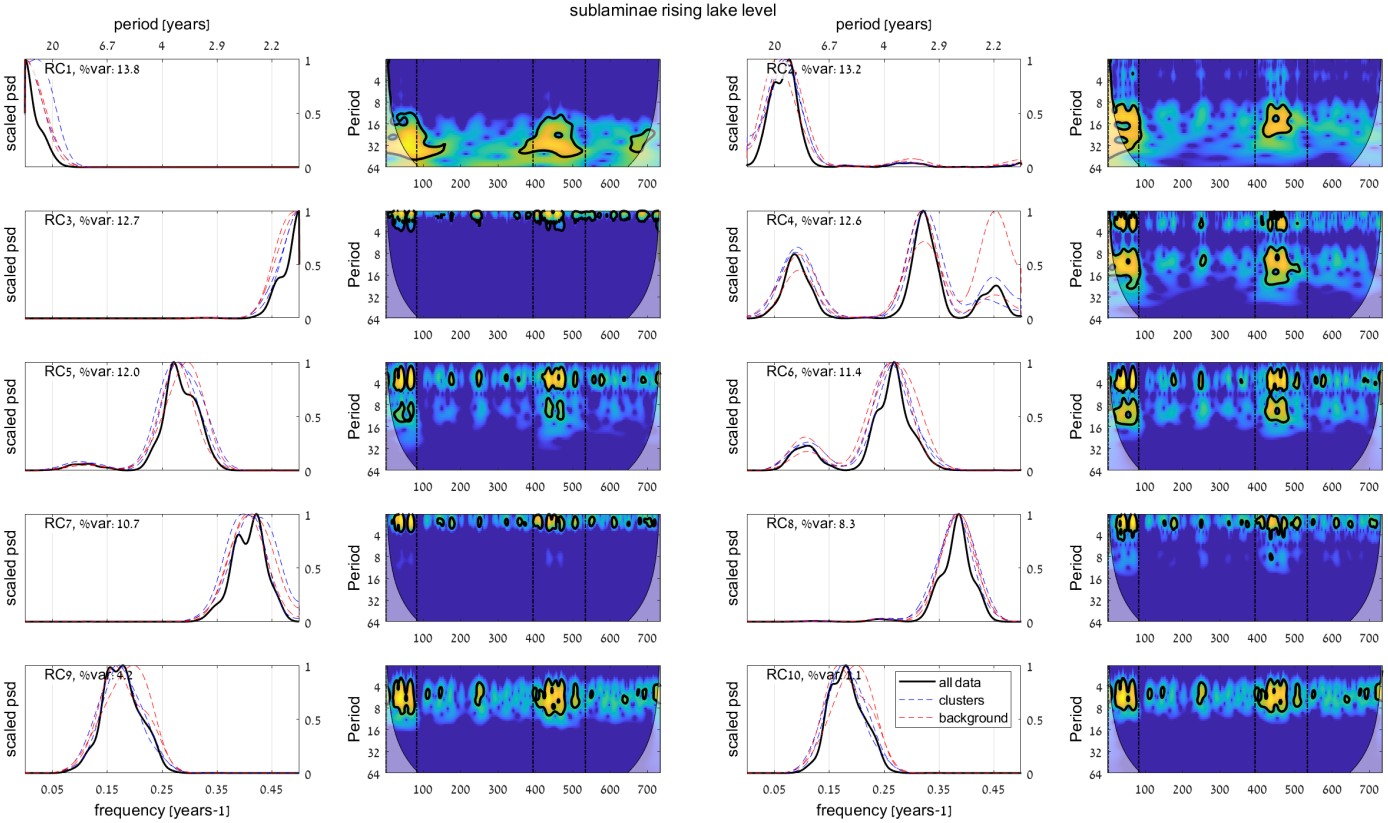

Figure S11 – Welch periodogram and wavelet analyses for the SSA RCs 1-10 of the sublaminae data during lake level rise .The periodograms were calculated using a Hamming window of 25 years length with 50% overlap, and wavelet analyses were carried out after normalizing to zero mean and a unity standard deviation.

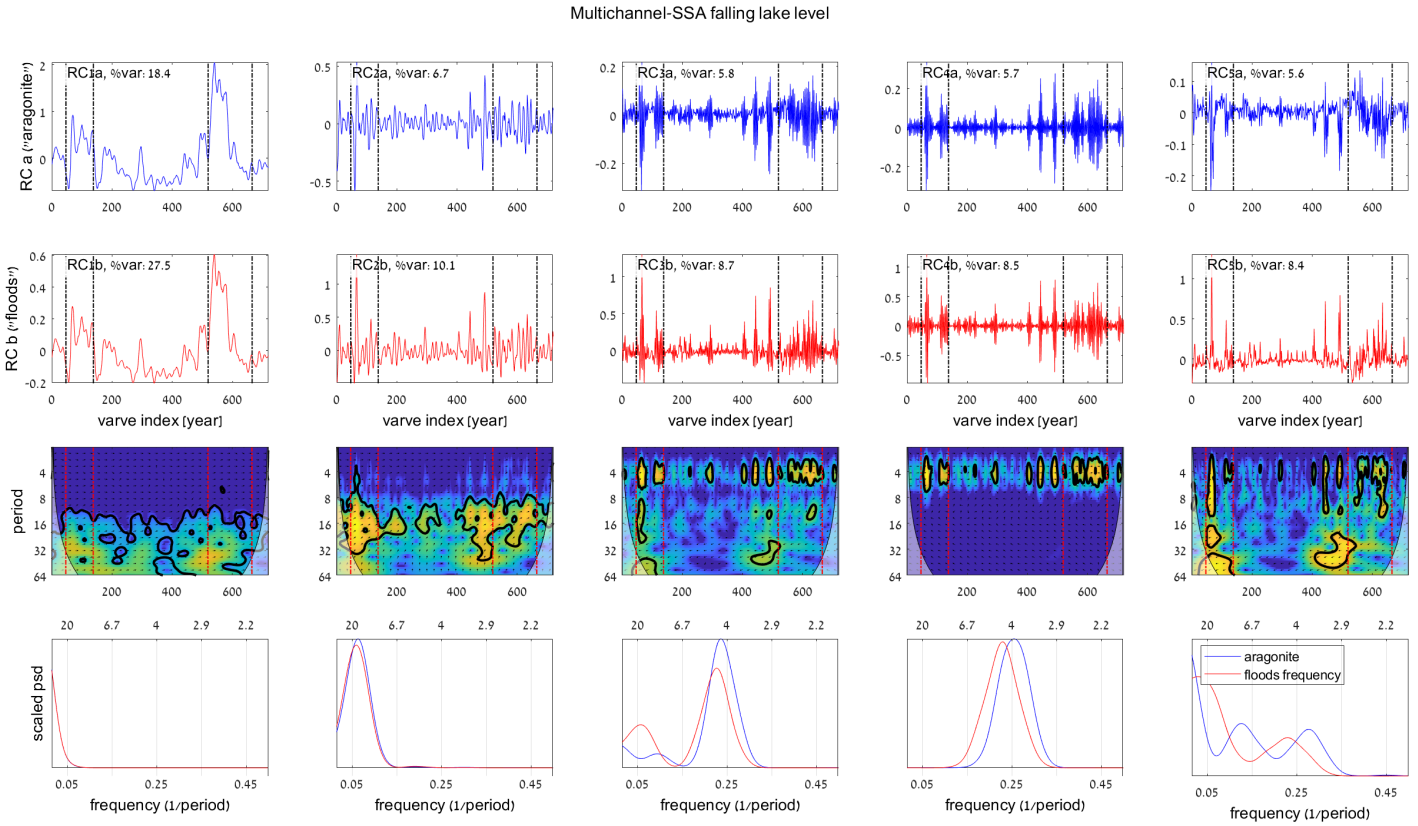

Figure S12 – Multichannel SSA of the aragonite (blue) and flood frequency (red) data. First two rows depict the reconstructed components of the M-SSA analysis for the data during falling lake level. The % of explained variance by each RC is depicted in each subplot. The third and fourth rows depict the cross-wavelet analysis of each of the two corresponding RCs, and the corresponding welch periodogram for the two channels. The periodograms were calculated using a Hamming window of 30 years with 50% overlap, and wavelet analyses were carried out after normalizing to zero mean and a unity standard deviation.

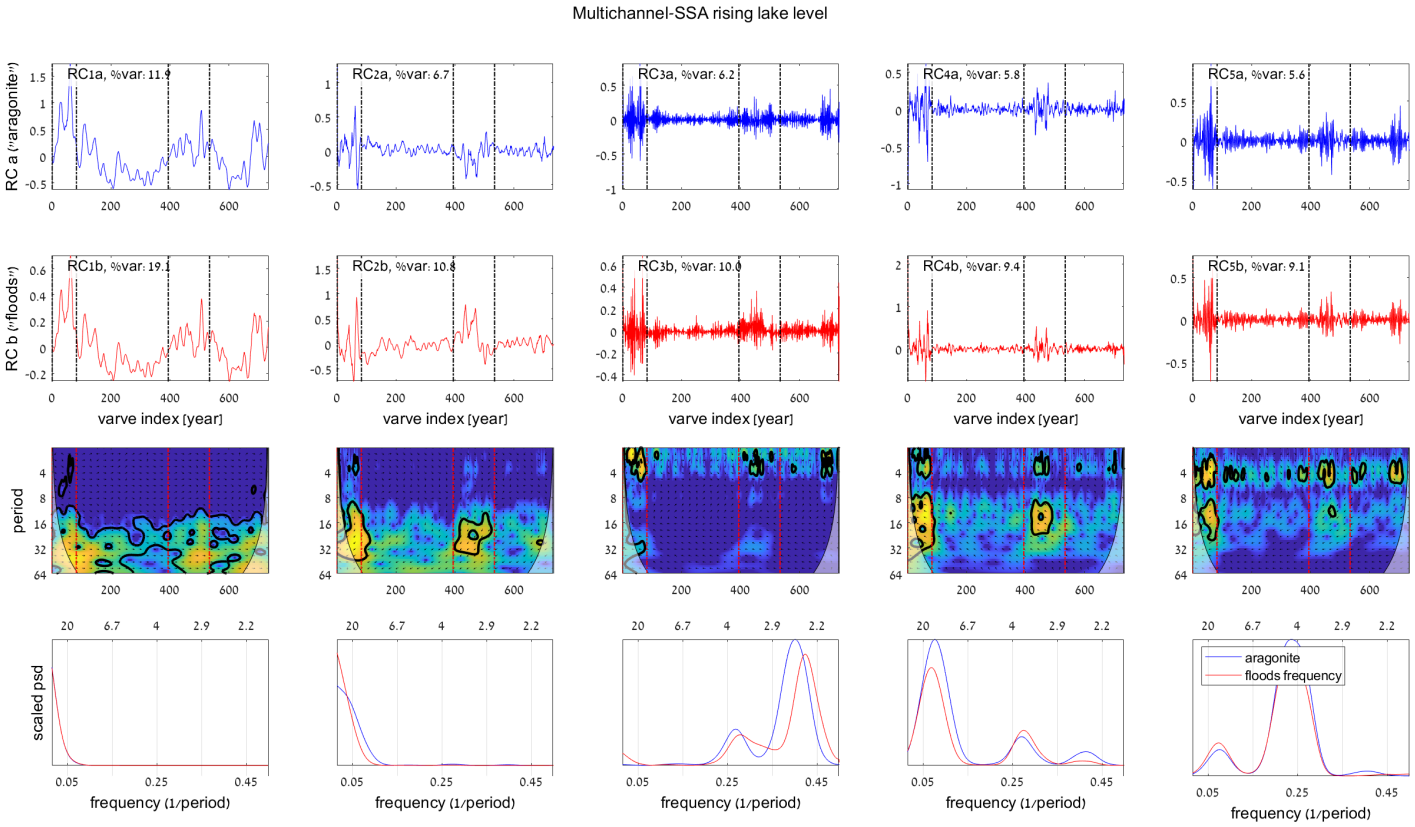

Figure S13 – Multichannel SSA of the aragonite (blue) and flood frequency (red) data. First two rows depict the reconstructed components of the M-SSA analysis for the rising lake level (Figure S 12). The % of explained variance by each RC is depicted in each subplot. The third and fourth rows depict the cross-wavelet analysis of each of the two corresponding RCs, and the corresponding welch periodogram for the two channels. The periodograms were calculated using a Hamming window of 30 years length and 50% overlap, and wavelet analyses were carried out after normalizing to zero mean and a unity standard deviation.

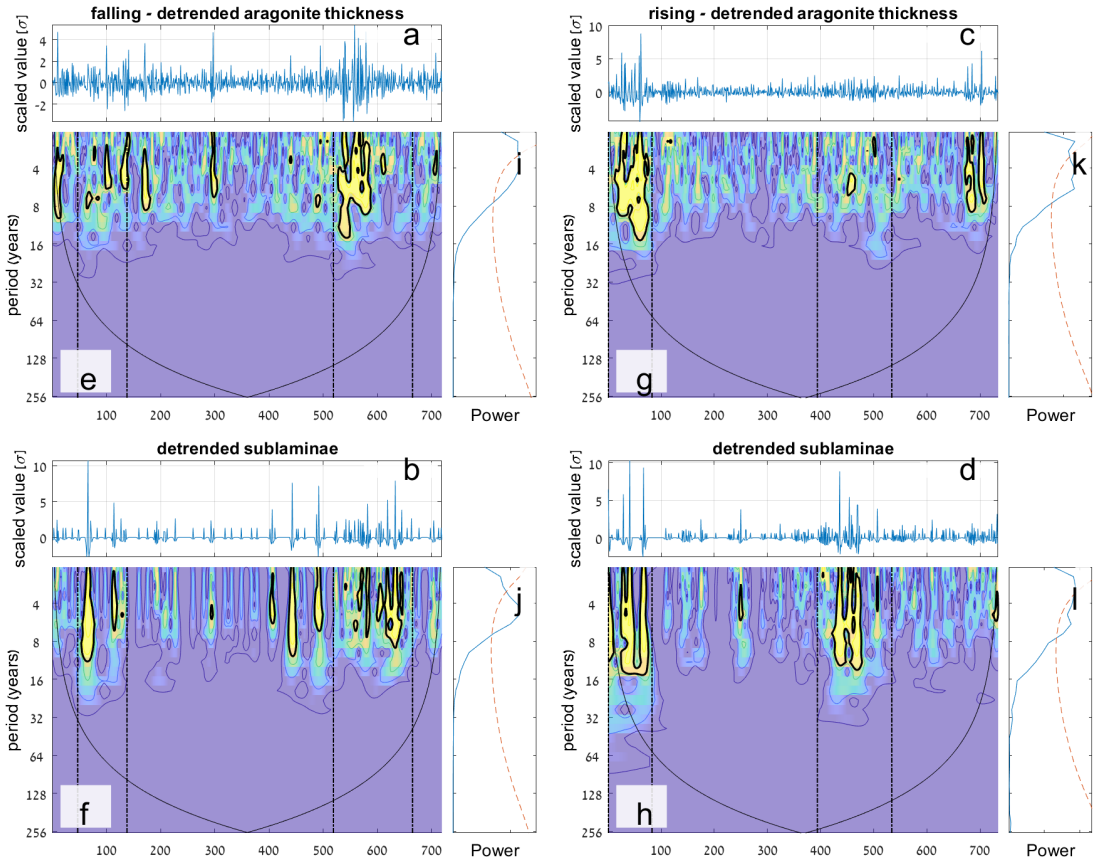

Figure S14 – wavelet and global-wavelet spectra of detrended aragonite thickness and flood frequency during falling (left) and rising (right) episodes. Periodicities with significance level above 0.95 (alpha=0.05) are depicted by a black line. Each triplot section depicts the data after normalization (a-d), the wavelet spectra (e-h) and the global wavelet spectra (blue) compared against a background red noise estimate (dashed red, i-l) Vertical dashed lines depict clusters identified as episodes of increased flood frequency.

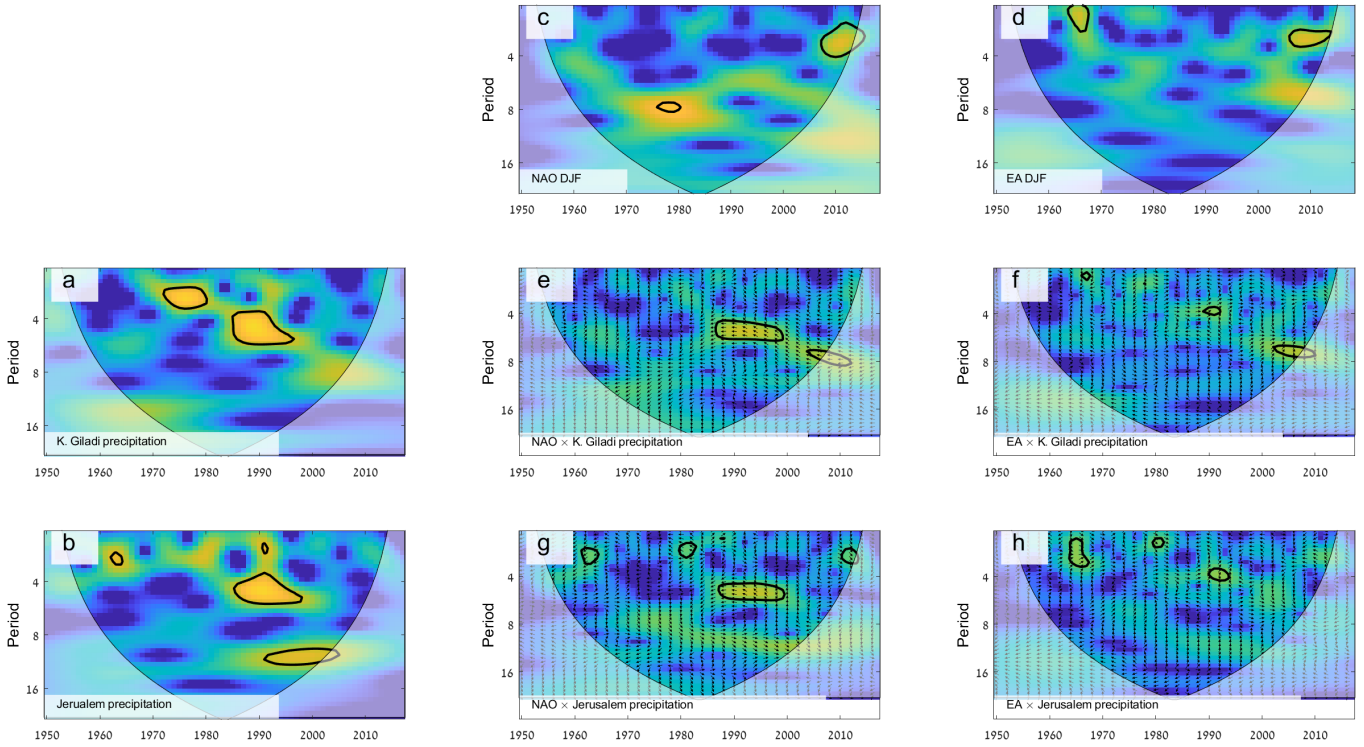

Figure S15 – wavelet (a-d) and wavelet (e-h) analyses of modern annual precipitation in Kfar Giladi (a) and Jerusalem (b), and the North Atlantic Oscillation (c) (NOAA, 2020) and Eastern Atlantic (d) indices. The analyses are presented only for the times span when all data is available (1950-2018). Areas with significance level above 0.9 (alpha=0.1) are depicted by a black line.

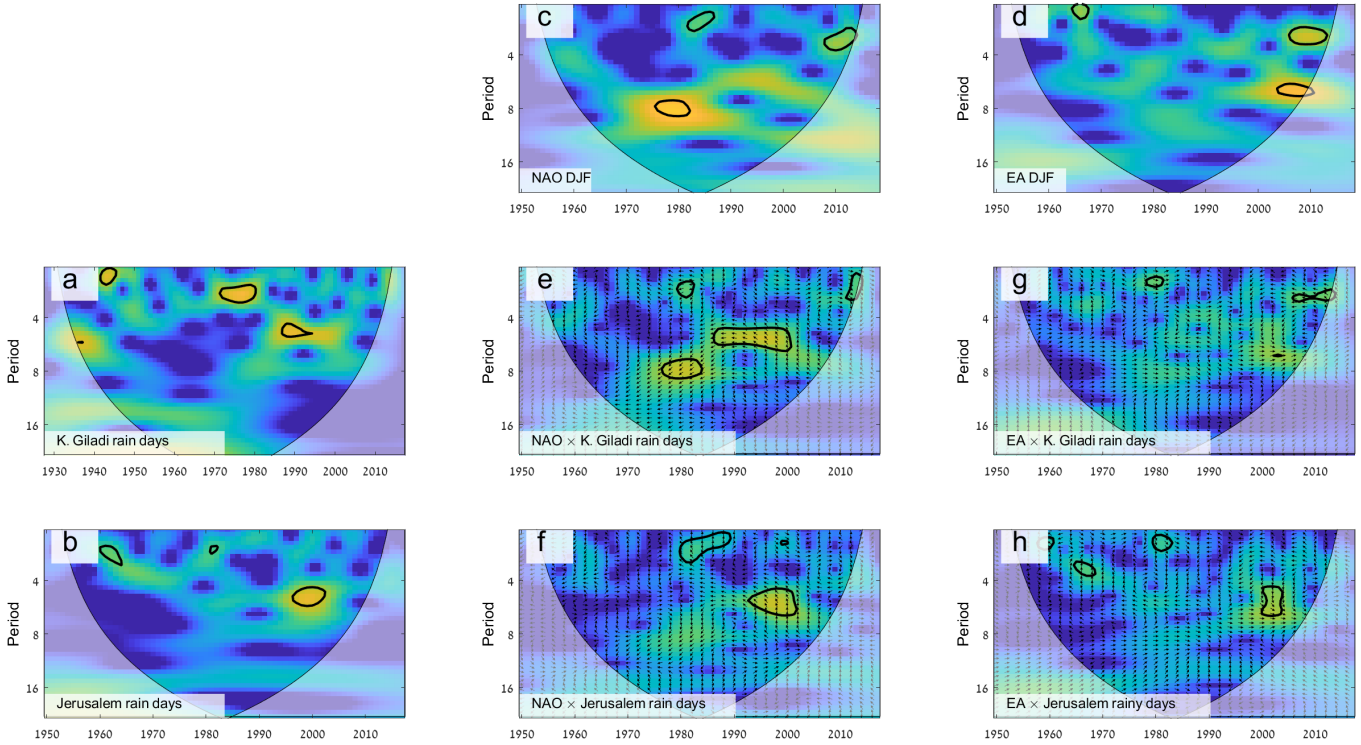

Figure S16 – wavelet (a-d) and cross-wavelet spectra (e-h) the number of rainy days and winter (DJF) NAO and EA measured at Kfar Giladi station, and winter (DJF) NAO (c) and winter (DJF) EA indices (d; NOAA, 2020). Arrows indicate significance above 0.5, and areas with significance level above 0.9 (alpha=0.1) are depicted by a black line.

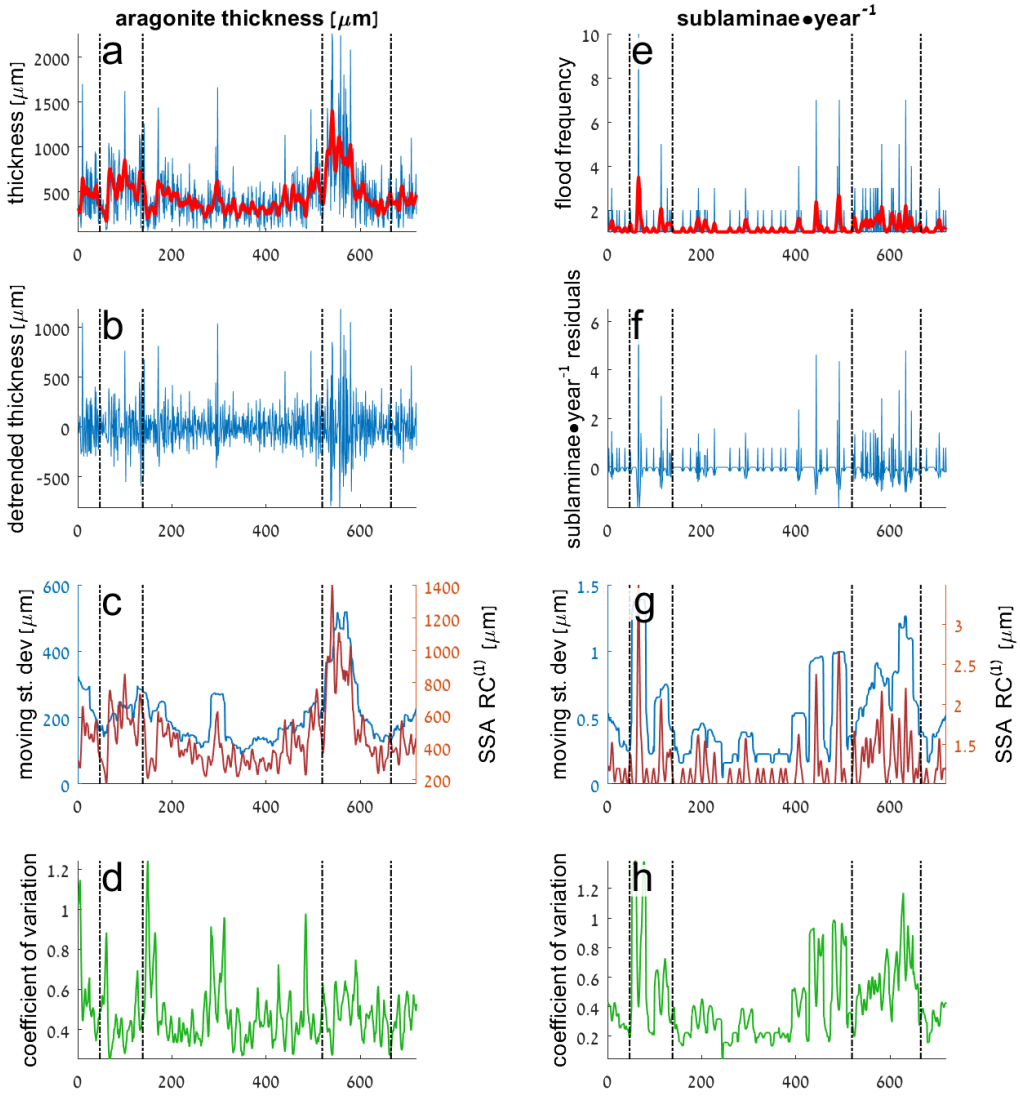

Figure S17 – selected running statistical properties of aragonite laminae (a-d) and flood frequency (e-h) for the studied lake level fall depicting the measured data (a,e), the residuals (after subtracting the $RC^{(1)}$) (c,f), $RC^{(1)}$ and running std. deviation (30 years window), and the coefficient of variation calculated by dividing the running std. deviation by $RC^{(1)}$ (d,h).

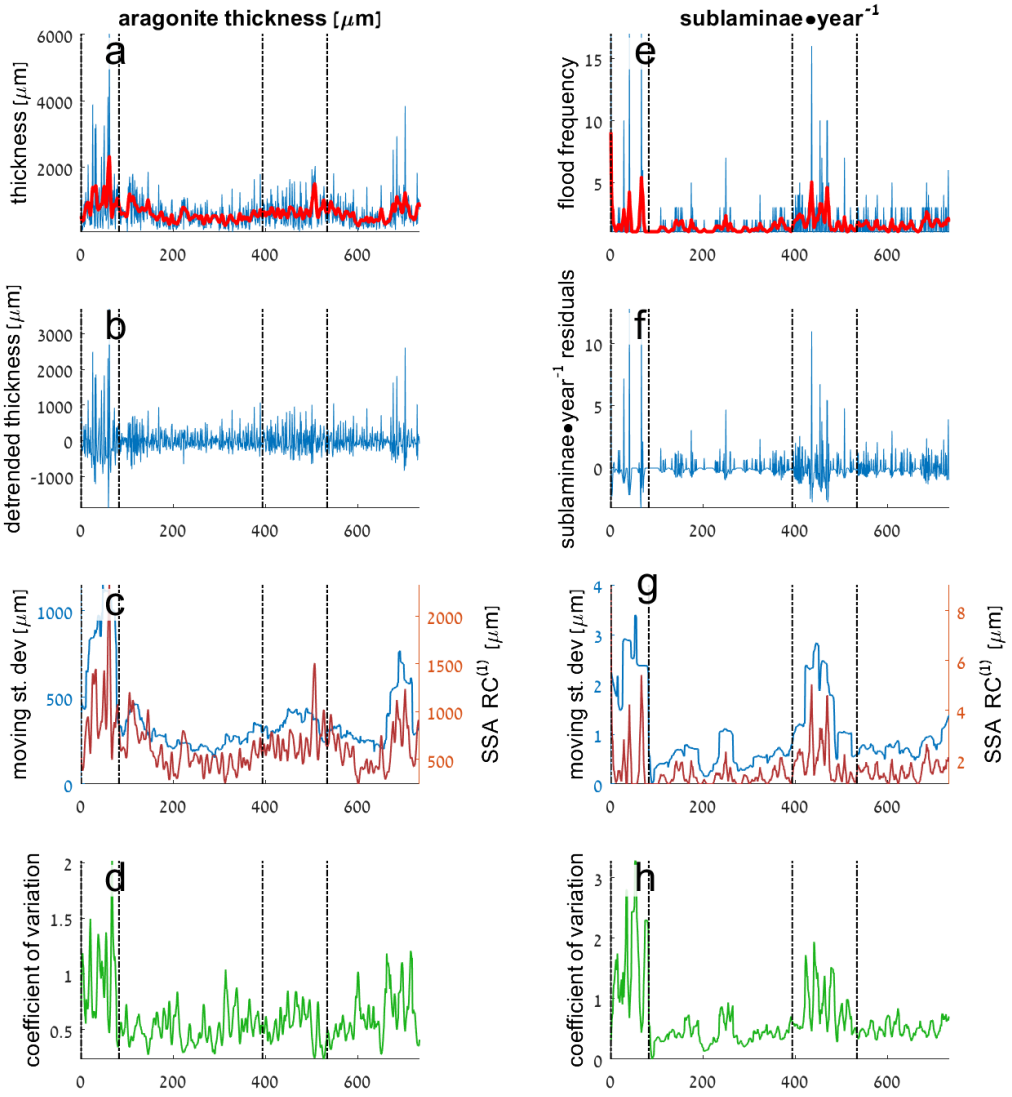

Figure S18 – selected running statistical properties of aragonite laminae (a-d) and flood frequency (e-h) for the studied lake level rise depicting the measured data (a,e), the residuals (after subtracting $RC^{(1)}$) (c,f), $RC^{(1)}$ and running std. deviation (30 years window), and the coefficient of variation calculated by dividing the running std. deviation by $RC^{(1)}$ (d,h).

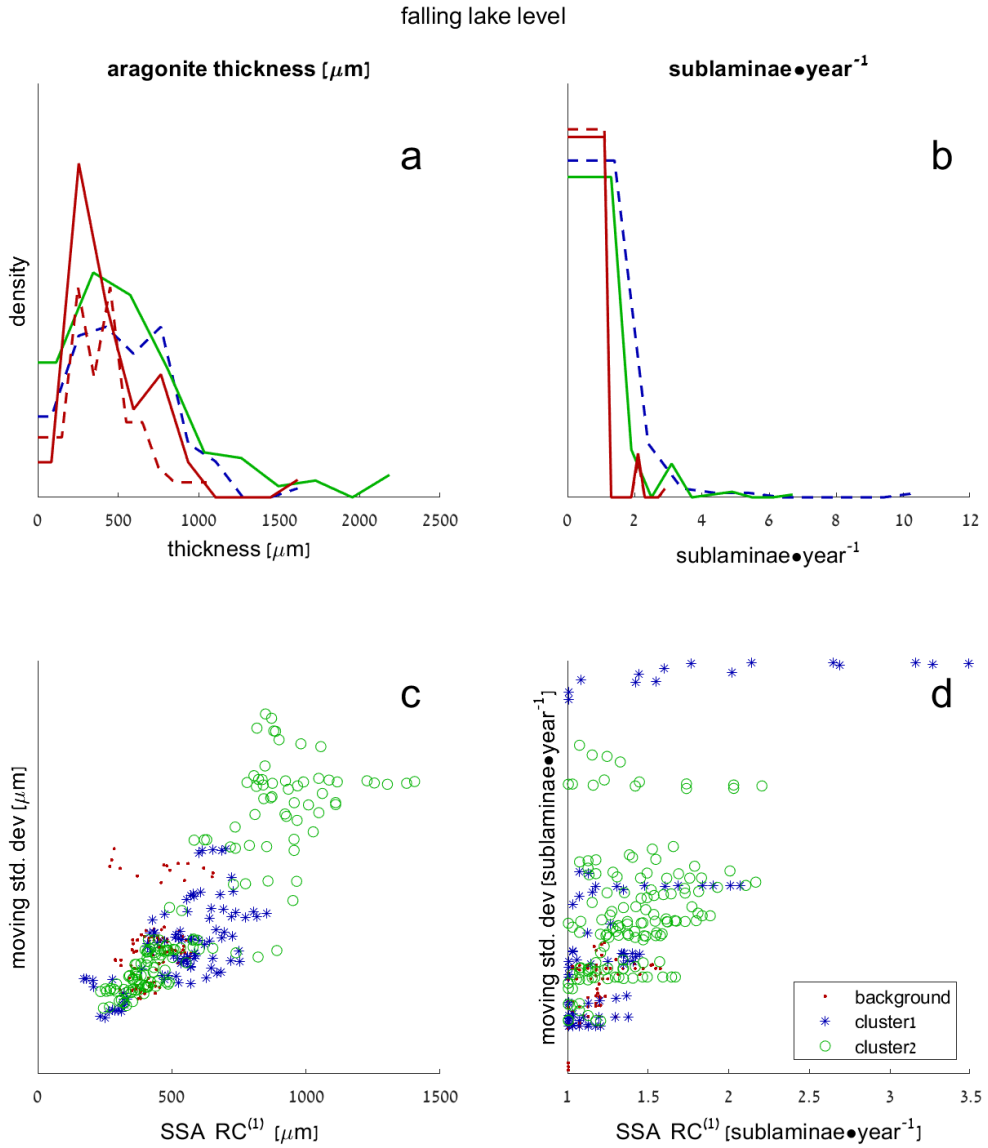

Figure S19 – distributions (a,b) and scatter (c,d) of statistical properties during studied falling lake level. Note the similarity between the first cluster and background intervals.

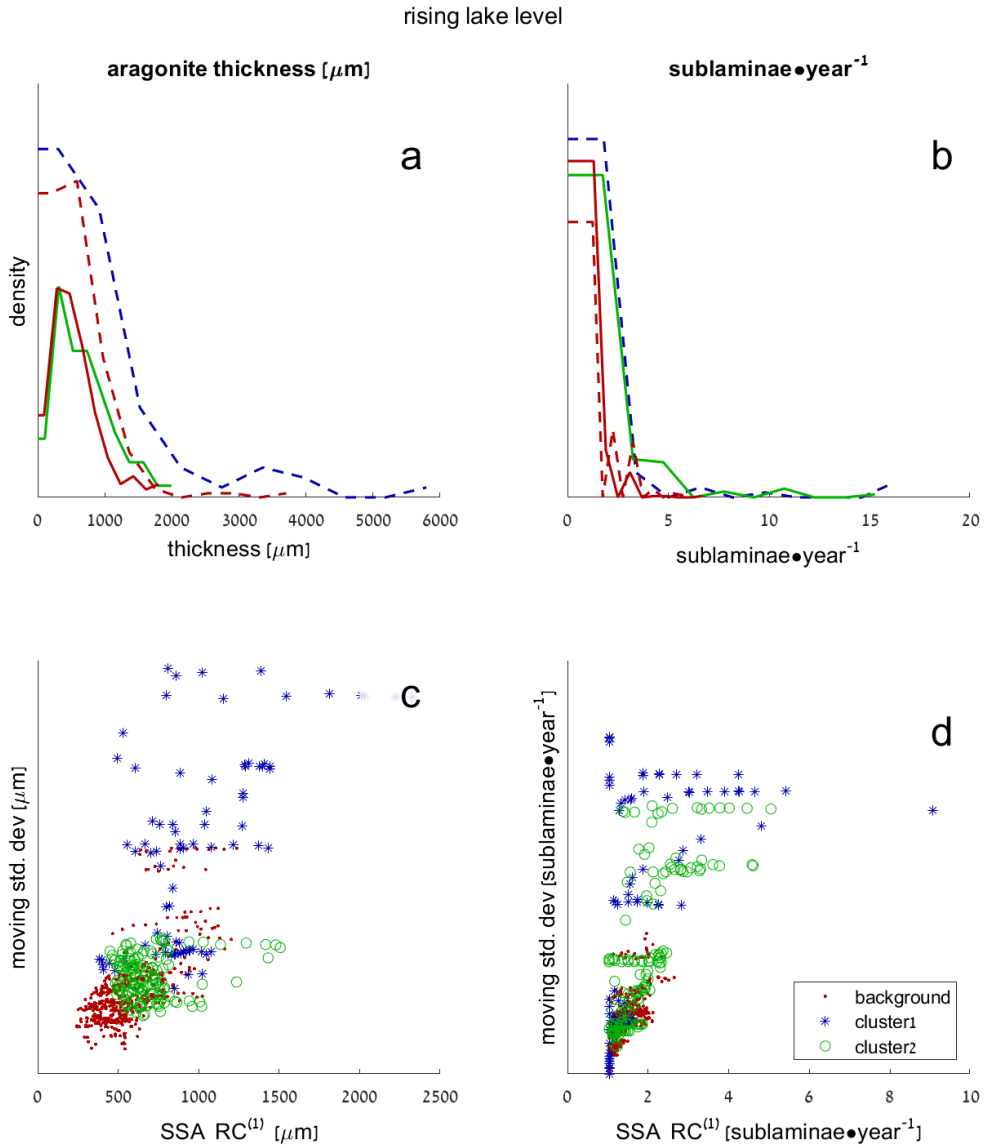

Figure S20 – distributions (a,b) and scatter (c,d) of statistical properties during studied falling lake level. Note the dissimilarity between the first cluster and the background intervals, and the similarity between the second cluster and the background intervals.

References

Broomhead, D. S. and King, G. P.: Nonlinear phenomena and chaos, Qual. Anal. Exp. Dyn. Syst. Malvern Sci. Ser. Bristol, UK, 113–144, 1986.

Ghil, M., Allen, M. R., Dettinger, M. D., Ide, K., Kondrashov, D., Mann, M. E., Robertson, A. W., Saunders, A., Tian, Y., Varadi, F. and Yiou, P.: Advanced spectral methods for climatic time series, Rev. Geophys., 40(1), 3-1-3–41, doi:10.1029/2000RG000092, 2002.

Haw, J. Y., Assad, S. M., Lance, A. M., Ng, N. H. Y., Sharma, V., Lam, P. K. and Symul, T.: Maximization of Extractable Randomness in a Quantum Random-Number Generator, Phys. Rev. Appl., 3(5), 054004, doi:10.1103/PhysRevApplied.3.054004, 2015.

Marchand, P. and Marmet, L.: Binomial smoothing filter: A way to avoid some pitfalls of least-squares polynomial smoothing, Rev. Sci. Instrum., 54(8), 1034–1041, doi:10.1063/1.1137498, 1983.

NOAA: Climate Prediction Center, [online] Available from: https://www.cpc.ncep.noaa.gov/data/teledoc/ea.shtml (Accessed 29 July 2020), 2020.

Supplementary 2 – A non-parametric Monte Carlo procedure for estimating cluster significance

The following non-parametric Monte Carlo procedure was developed to investigate the likelihood of randomly observing the time interval between floods-rich episodes (i.e., clusters):

1. The normalized running sum of sublaminae was calculated for the two observed flood events series (Equation S2-1).

Eq. S2-1:
$$y_{w(i)} = \begin{cases} i < \frac{w}{2} & NaN \\ \frac{w}{2} < i < N - \frac{w}{2} & \frac{\sum n_j}{\widehat{y_w}}, \left[i - \frac{w}{2} \le j \le i + \frac{w}{2}\right] \\ i > N - \frac{w}{2} & NaN \end{cases}$$

Where $y_{w(i)}$ is the normalized running sum, i is the location index ranging between 1 and N, N is the number of data points in each series, $\sum n_j$ is the sum of sublaminae count over the range between $\left[i - \frac{w}{2} \le j \le i + \frac{w}{2}\right]$, w is the window width for calculating the $y_{w(i)}$ statistic, ranging from 10 to 300 by 10 years steps (w =[10,20,30,…,290,300]) , and $\widehat{y_w}$ is the mean normalized sum of n for window width w. Thus, $y_{w(i)}$ values larger than unity indicate values concentrations of flood-rich years which are above mean for the selected w, and $y_{w(i)}$ values lower than one indicate values below the mean reflecting flood-poor years.

2. After calculating the $y_{w(i)}$ statistic, a peak detection algorithm was used to identify local $y_{w(i)}$ maxima for the width of the window (Fig. S2-1). In case where no peaks were detected the largest y_i value was selected.

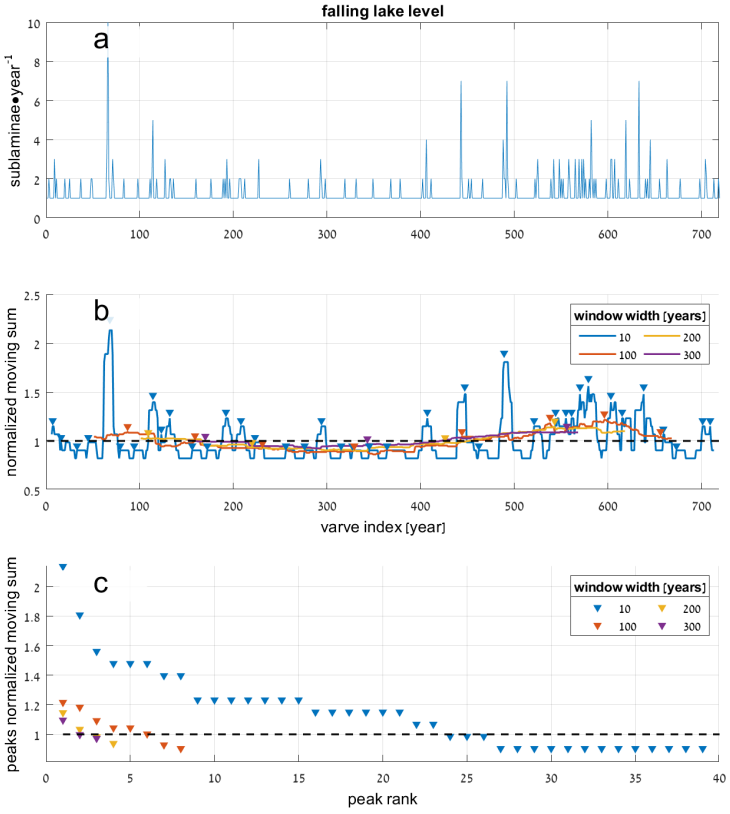

Figure S2-1 – a demonstration of the statistic developed for identifying clusters in the time series. a) the studied time series of sublaminae. b) the $y_{w(i)}$ statistic calculated using several window widths. Values larger than one are above the mean level. Detected peaks are marked by a triangle. c) the $y_{w(i)}$ values of detected peaks sorted by their order, thus larger values appear first.

3. After calculating the $y_{w(i)}$ values of the studied series for all window widths, each series was randomly permutated 10,000 times and the calculation was repeated, resulting in a vector of 10,000 values for each peak values for every window width. Naturally, the number of identified peaks decreases as the width of the window increases, and the $y_{w(i)}$ value of the peak decreases with its rank (Fig. S2-2).

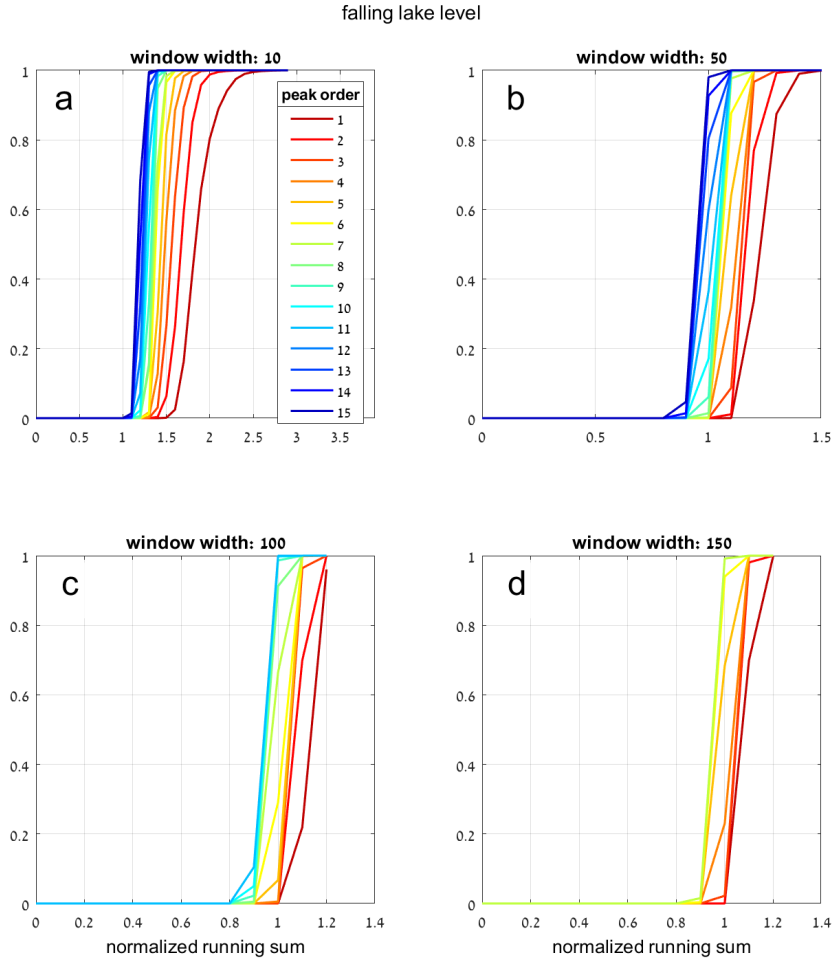

40 **Figure S2-2 – distributions of $y_{w(i)}$ values of peaks calculated for 10,000 randomly permutated series depicting the values of the random series for four representative window widths. Note the decrease in both $y_{w(i)}$ values and number of identified peaks with increasing window width.**

4. After calculating the distribution for each peak order (up to rank 15) and window width the observed values were compared to those calculated for the randomly permutated series (Fig. S2-3). The 50th, 95th and 99th percentile were calculated, and observed peaks were considered significant at α=0.05 when observed $y_{(w,i)}$ values were higher than the values calculated for the 95th percentile for the peak rank and window width (Fig. S2-4).

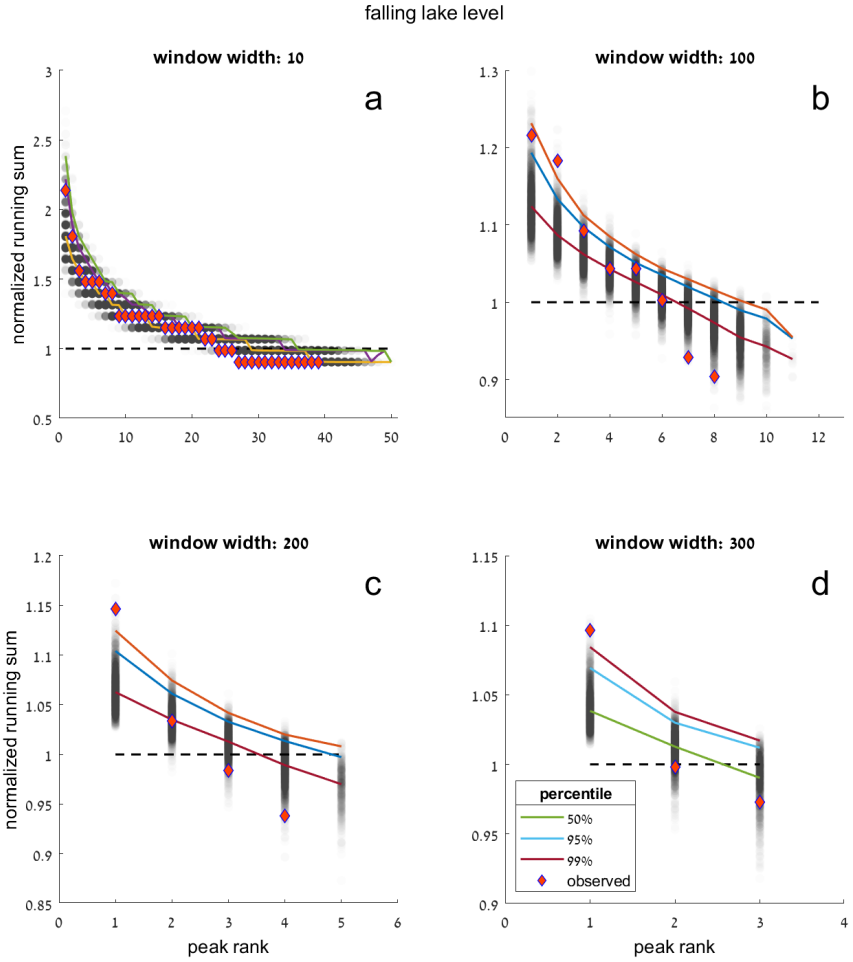

Figure S2-3 – distributions of $y_{w(i)}$ values of peaks calculated for 10,000 randomly permutated series depicting the values of the random series (grey circles), the median, 95th and 99th percentile for each peak order (colored lines), and the observed value in the studied series. Rare values and significant at an α level of 0.05 plot above the 95th percentile of the randomly permutated series, whereas common and non-significant values appear below the 95th percentile.

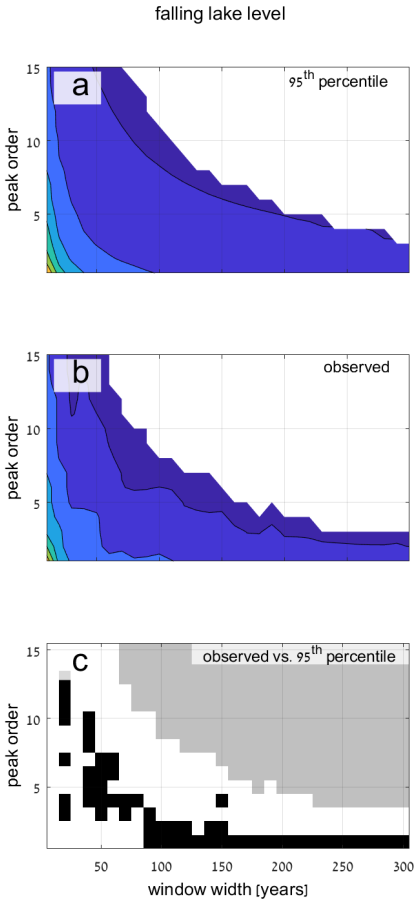

Figure S2-4 – a) the resulting $y_{(w,i)}$ values of the 95th percentile for every peak rank (1-15) and window width (10-300). b) the observed $y_{w(i)}$ values for every peak rank (1-15) and window width (10-300). c) a binary diagram indicating where observed $y_{w(i)}$ values are higher than the calculated 95th percentile of 10,000 randomly permutated series, and are thus statistically significant at α=0.05 (black pixels) or non-significant (white pixels). Missing values, where not enough peaks were detected to calculate the 95th percentile are coded grey.

5. Finally, the ranges of the statistically significant peaks for α=0.05 were plotted over the data to indicate where significant peaks of the first three ranked peaks of window widths between 50 and 300 occur (Fig. S2-5).

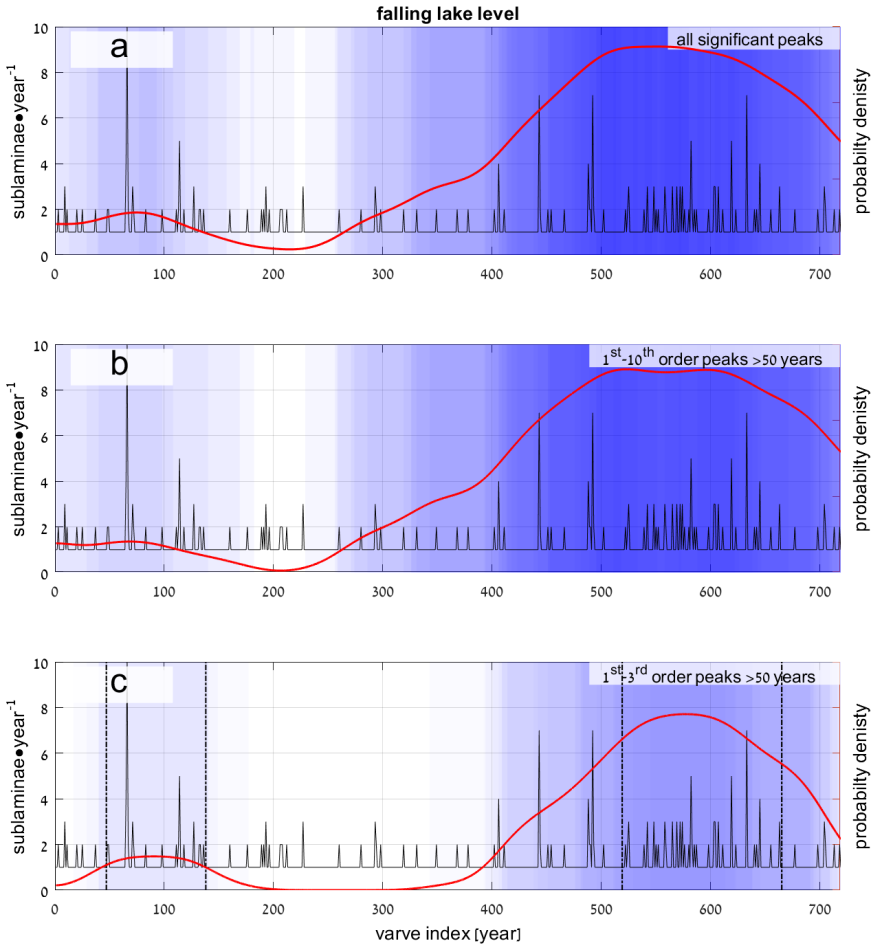

Figure S2-5 – the location of statistically significant peaks at α=0.05 depicted as semi-transparent shading for: a) all identified statistically significant peaks, b) only peaks detected for window widths longer than 50, and c) for the top five ranking peaks of window widths ranging between 50 and 300. The overall calculation suggests two clusters between ~50-150 and ~550-650. The red line depicts the probability of the summed identification of clusters by all window widths depicted in each plot. The identified refined clusters are marked by dashed vertical lines.

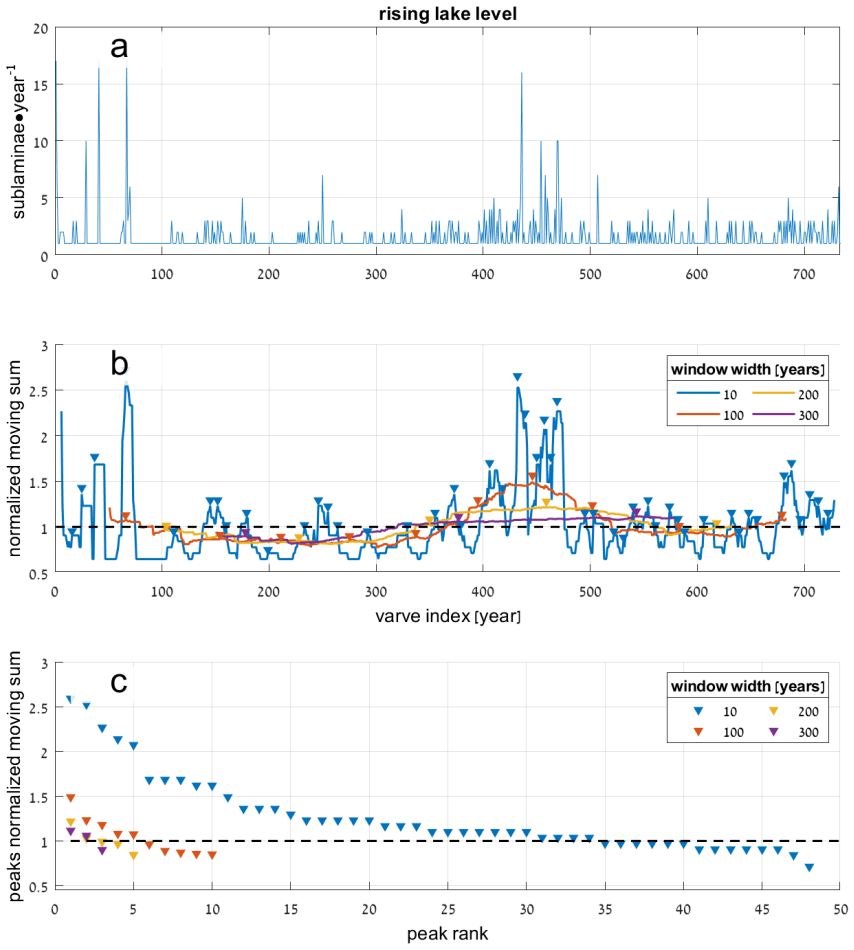

Figure S2-6 – same as Fig. S2-1 but for the studied lake level rise.

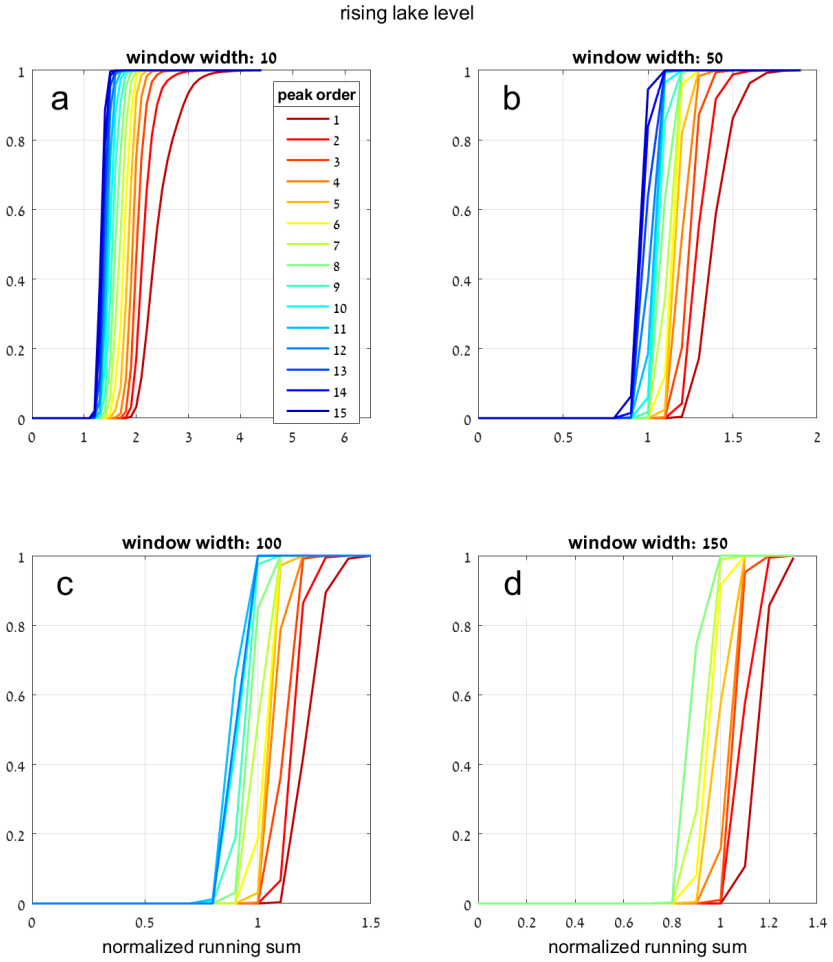

75 **Figure S2-7 - Fig. S2-2 but for the studied lake level rise.**

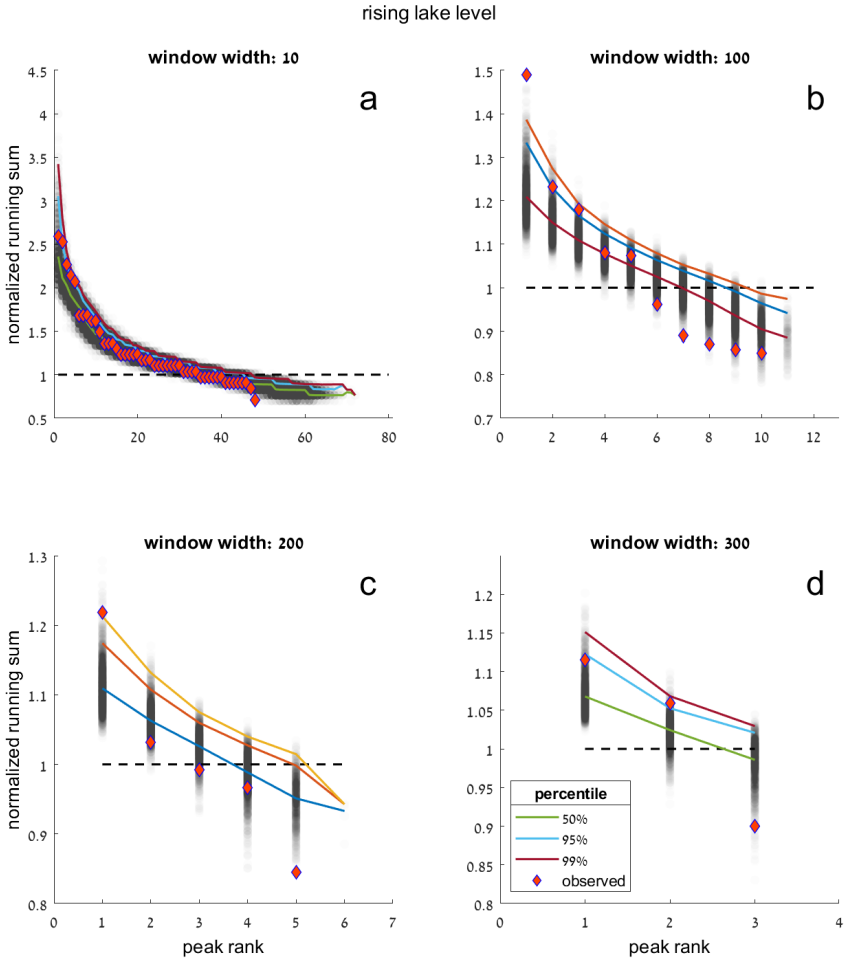

Figure S2-8 - Fig. S2-3 but for the studied lake level rise.

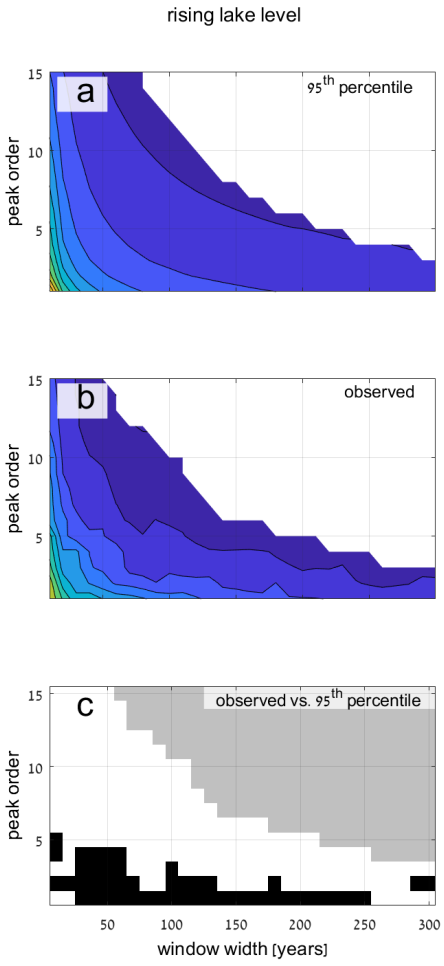

Figure S2-9 - Fig. S2-4 but for the studied lake level rise.

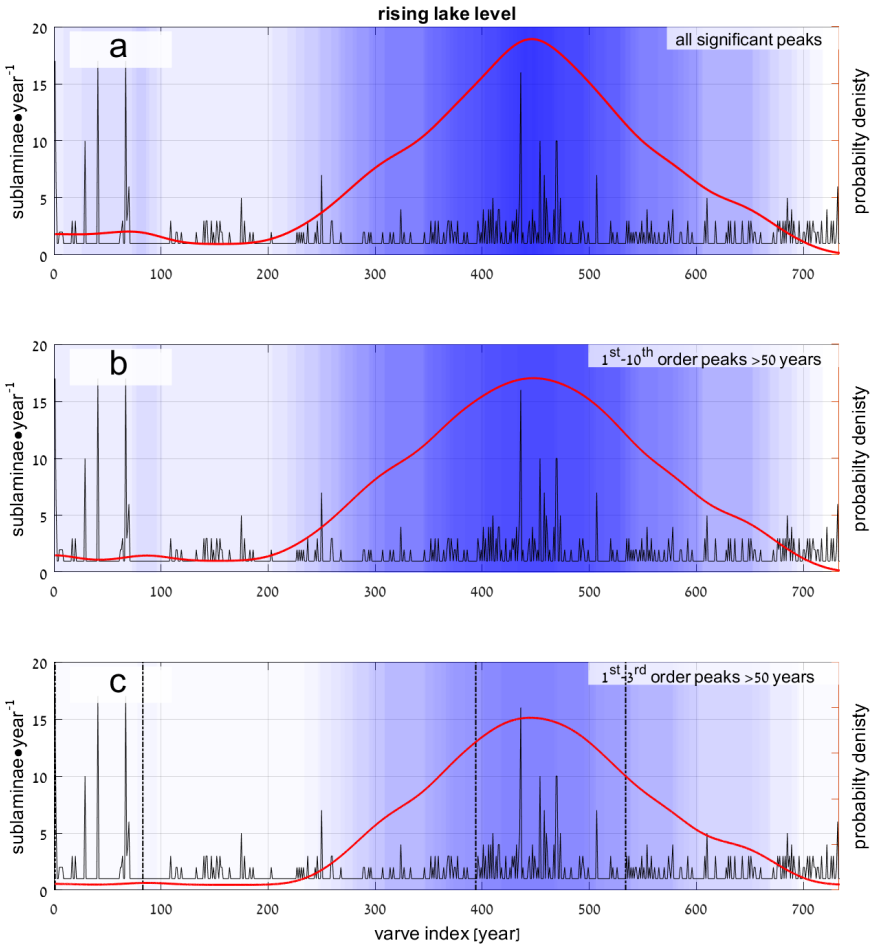

80

Figure S2-10 - Fig. S2-5 but for the studied lake level rise.